Journal of Catalysis 396 (2021) 136–147

Contents lists available at ScienceDirect

Journal of Catalysis

journal homepage: www.elsevier.com/locate/jcat

Unravelling the effect of impurities on the methanol-to-olefins process in waste-derived zeolites ZSM-5

Nikolaos Nikolopoulos, Robin G. Geitenbeek, Gareth T. Whiting, Bert M. Weckhuysen *

Inorganic Chemistry and Catalysis, Debye Institute for Nanomaterials Science, Utrecht University, Universiteitsweg 99, 3584 CG Utrecht, the Netherlands

ARTICLE INFO

Article history:
Received 13 December 2020
Revised 15 February 2021
Accepted 16 February 2021
Available online 25 February 2021

Keywords:
Waste valorization
Waste-derived zeolites
ZSM-5
Impurities
Methanol-to-hydrocarbons
MTH
Operando UV–Vis DRS

ABSTRACT

One of the main challenges in the next decades for the chemical industry is the valorization of low-grade industrial waste streams into valuable materials, as their increasing amount can have a major environmental impact. For example, in copper mining industry, waste flotation tailings can be valorized into solid acid catalysts, such as zeolites. Numerous studies have shown that modification of zeolites by metal ions has a positive effect in their catalytic performance. However, the presence of impurities in waste-derived materials is usually disregarded. In this work, the influence of impurities in waste-derived zeolites ZSM-5 on the physicochemical properties and the catalytic performance in methanol-to-hydrocarbons (MTH) reaction was investigated. Flotation tailings from copper industry, mainly consist of SiO_2 as quartz, next to Ca, Mg and Fe species. By altering the pH in the SiO_2 precipitation step, the impurities content in the waste-derived zeolites ZSM-5 could be controlled. Chemical analysis confirmed the presence of Fe, Ca and Mg in low concentrations in the waste-derived samples. UV–Vis Diffuse reflectance spectroscopy (DRS) and electron paramagnetic resonance (EPR) showed the presence of different Fe species in the waste-derived samples in the form of isolated Fe^{3+}, oligomeric Fe_xO_y species and some extended Fe_2O_3-like clusters. Temperature programmed desorption (TPD) of NH_3 and infrared (IR) spectroscopy measurements after CO and pyridine adsorption were used in order to probe the effect of the cations present in the acidity of the waste-derived materials. It was found that the zeolite material with a higher amount of metal impurities contained less Brønsted acid sites and more Lewis acid sites. Catalytic testing showed that the metal impurities had a positive influence on the overall catalyst stability and the yields towards ethylene and propylene were respectively 8% and 6% up. Meanwhile, *operando* UV–Vis DRS showed the influence of impurities on the catalytic mechanism, as its increase led to the formation of less hydrocarbon pool species. This study not only show that waste can be transformed into value-added materials, namely a zeolite-based catalyst material, but also that the impurities present in the waste can further improve the catalytic performance of the solid catalyst.

1. Introduction

Nowadays, the enormous amount of industrial solid waste, e.g., from metallurgical and incineration plants, draws global attention as it can be dangerous for the environment and cause serious health problems to humans [1,2]. Furthermore, raw materials are also limited, resulting in a drive for a waste-free production cycle of our daily materials and goods. By developing methods to valorize waste and turn them into value-added materials, not only can waste production be reduced, but a new source of raw materials becomes available, thereby providing the necessary steps towards a more circular economy.

A huge hazard for the environment, but also a big potential for waste valorization, lies in the mining industry where flotation tailings are produced, which are waste materials produced by the separation of the valuable ore fraction from the non-economic fraction during processing. These waste flotation tailings can react with water and oxygen when exposed to atmospheric conditions and as a result they produce acidic wastewater and sulfates [3]. These deposits mainly consist of many different minerals, like aluminum oxide (Al_2O_3), calcium oxide (CaO), ferric oxide (Fe_2O_3), calcite ($CaCO_3$) and silicon oxide (SiO_2) and also precious metals (e.g., Ni, Co, Cu, Zn, Au and Ag) [1–6]. Recently, it has been shown that precious as well as economically important metals can be extracted and utilized for the manufacturing of adsorbents and solid catalysts [3,7,8].

* Corresponding author.
E-mail address: b.m.weckhuysen@uu.nl (B.M. Weckhuysen).

https://doi.org/10.1016/j.jcat.2021.02.015
0021-9517/

Researchers have also tried to reuse silicon-rich wastes (e.g., fly ash and coal fly ash) as alternative source for the manufacturing of heterogeneous catalysts. There are numerous studies in which fly ash is used as catalytic support [9–13]. Moreover, coal fly ash has been used as raw material for the synthesis of porous materials, such as MCM-41, Al-MCM-41 and SBA-15, and used for different catalytic applications [7]. In a recent study of *Li et al.*, fly ash-derived SBA-15 was used as a support material for Fe and Mn oxides, which can be used as solid catalysts for the selective catalytic reduction of NH_3 (NH_3-SCR)[14]. Furthermore, using similar waste streams, silica aerogel and adiabatic foam were made [7]. In addition to the synthesis of support oxides, different types of zeolites have been prepared, such as zeolite X (FAU), Y (FAU), A (LTA), P (GIS), ZSM-5 (MFI), phillipsite (PHI) and SAPO-34 (CHA), using fly ash or similar types of waste streams via a conventional hydrothermal method [7,15]. Missengue *et al.* used coal fly ash as a precursor for the synthesis of zeolite ZSM-5 and its catalytic performance was tested in the methanol-to-hydrocarbons (MTH) reaction. By further treating the waste-derived zeolite ZSM-5 with oxalic acid, full methanol conversion for 15 h could be achieved with a 35% selectivity towards propylene [16]. In a follow-up study of Missengue *et al.*, the physicochemical characteristics of zeolite ZSM-5, derived from acid treated coal fly ash and fused coal fly ash, were compared. Furthermore, the impact of tetrapropylammonium bromide, 1,6-hexanediamine and 1-propylamine as structure-directing agents (SDA) on the physicochemical properties and the catalytic performance in the MTH reaction of the waste-derived zeolite ZSM-5 materials were examined. It was concluded that the use of 1,6-hexanediamine resulted in a decrease in the zeolite crystal size and the obtained material was found to be more stable in the MTH process [17].

However, waste-derived zeolite-based materials can contain impurities originating from the initial waste, which are usually neglected. *Chareonpanich et al.* reported the synthesis of zeolite ZSM-5 derived from lignite fly ash and rice husk ash [18]. The materials made were compared in terms of catalytic activity in CO_2 hydrogenation. It was shown that metal impurities slightly boosted CO_2 conversion and increased the yield of C_2-C_3 hydrocarbons. Recently, zeolite Na-X was synthesized from waste coal fly ash and it was observed that iron oxide was incorporated in the zeolite matrix [19,20]. Although the catalytic performance in the oxidation of volatile organic compounds (VOCs) seemed to improve for these waste-derived zeolites, the effect of impurities in waste-derived zeolites on their catalytic performanes is still poorly understood.

Each of the above literature studies demonstrate the intrinsic challenges associated with waste streams as a potential source for the synthesis of solid catalysts, including zeolites. Furthermore, the effect of the impurities in waste-derived zeolites on its physicochemical properties and catalytic performance is not yet well established. In this study, the effect of the type and amount of impurities, originating from flotation tailings from the copper industry, on the physicochemical properties and the catalytic performance of waste-derived zeolite ZSM-5 was investigated. Pretreatment steps were the key to control the impurities in the waste-derived zeolites. Tuning the pH during SiO_2 precipitation resulted in changes in the content of impurities in the formed zeolite. An in-depth characterization revealed the influence of the impurities on the physicochemical properties of the waste-derived ZSM-5 zeolites. Chemical analysis confirmed the impurities present in the waste-derived zeolite materials. The morphology and porosity are influenced by the impurities content (e.g., Fe, Ca, Mg and Na) as shown by scanning electron microscopy (SEM) and Ar physisorption. Moreover, the remaining impurity cations had an effect on the acidic properties, as assessed by ammonia temperature programmed desorption (NH_3-TPD) and FT-IR spectroscopy with CO and pyridine as probe molecules. Last but not least, the waste-derived zeolites were tested for their catalytic performance in the MTH reaction. It was found that impurities can have a great influence on the catalytic performances, as materials with higher amount of impurities showed a faster decrease in conversion due to the larger zeolite crystals formed, whilst it exhibited higher yields of light olefins (i.e., ethylene and propylene) because of the impurity-induced changes in its acidic properties, compared to the materials with a lower amount of impurities.

2. Experimental section

2.1. Chemicals and materials

The following chemicals, gases and materials were used: Ammonium nitrate (NH_4NO_3, 97%, Sigma Aldrich), hydrochloric acid (HCl, fuming 37%, Merck), sodium hydroxide (NaOH, 100%, EMSURE), sulfuric acid (H_2SO_4, >99.0%, EMSURE), tetrapropylammonium hydroxide (TPAOH, 1 M aq. solution, Alfa Aesar) and aluminum sulfate octadecahydrate ($Al_2(SO_4)_3$ $18H_2O$, >99.9%, Arcos Organics), pyridine (C_5H_5N, Merck, EMSURE), carbon monoxide (CO, Linde, >99%), aqua regia: a mixture of hydrochloric acid (HCl, fuming 37%, Merck) and nitric acid (HNO_3, 65%, Merck, EMSURE) in a ratio 3:1, methanol (Acros, HPLC grade, 99.99% pure), lithium borate (75%, Sigma-Aldrich), N_2 (Linde, 99.998%), He (Linde, >99%), Ar (Linde, 99.998%), fumed silica (CAB-O-SIL®, Cabot corporation). For reference purposes, we have used a commercial zeolite ZSM-5 sample (ACS Material) with a SiO_2/Al_2O_3 ratio of 38, a surface area of 380 m^2/g and an average particle size of 2 μm.

As shown in Scheme 1, Cu flotation tailings were milled and sieved in order to get a particle size less than 75 μm. ~12 g of Cu flotation tailings was calcined for 5 h at 700 °C in air and subsequently mixed with 400 mL of 3 M hydrochloric acid in a round flask refluxed at 100 °C for 2 h. The acid-treated Cu flotation tailings were separated by filtration under vacuum and washed until the pH of the filtrate was equal to 7 before drying at 120 °C for 12 h. The dried acid-treated Cu flotation tailings were then mixed with fine solid powder of NaOH in a mass ratio 1:1.5, respectively, and fused at 550 °C for 1 h. The alkali-fused material was subsequently mixed with 50 mL demineralized water for 24 h. The obtained mixture (solid and supernatant) was centrifuged. To the supernatant, an amount of 9 M H_2SO_4 was added until the pH was equal to 3 or 10. Because of the pH used, these materials were named sample S3 and sample S10, respectively. As a result, a gel had been formed, which was centrifuged and washed. The gel made was then dried at 120 °C for 12 h in air in order to obtain amorphous SiO_2.

For the synthesis of zeolite ZSM-5, the two different silica materials, prepared by precipitation at the two different pH values (i.e., pH = 3 and pH = 10) as well as a high purity fumed silica, were used as the source of silicon. The following procedure was used, while the mass ratios between Si, Al, Na, TPAOH and H_2O were 1.0:0.05:0.08:0.2:25. The proper amount of silica was mixed with demineralized water and 10 wt% NaOH and stirred at 80 °C for 2 h. Afterwards, TPAOH as template was added and the mixture was stirred and heated at 80 °C for 2 h. Afterwards, the solution was cooled to room temperature and $Al_2(SO_4)_3{\cdot}18H_2O$ was added. The mixture was stirred for 1 h at room temperature to homogenize the solution. The solution was then transferred in a 45 mL Teflon liner and put in a stainless steel autoclave in an oven at 180 °C for 84 h to perform a static hydrothermal zeolite synthesis. After this time, the autoclave was quenched in cold water to stop the synthesis reaction. The solid material obtained was separated from the supernatant. The derived solid was first dried at 120 °C

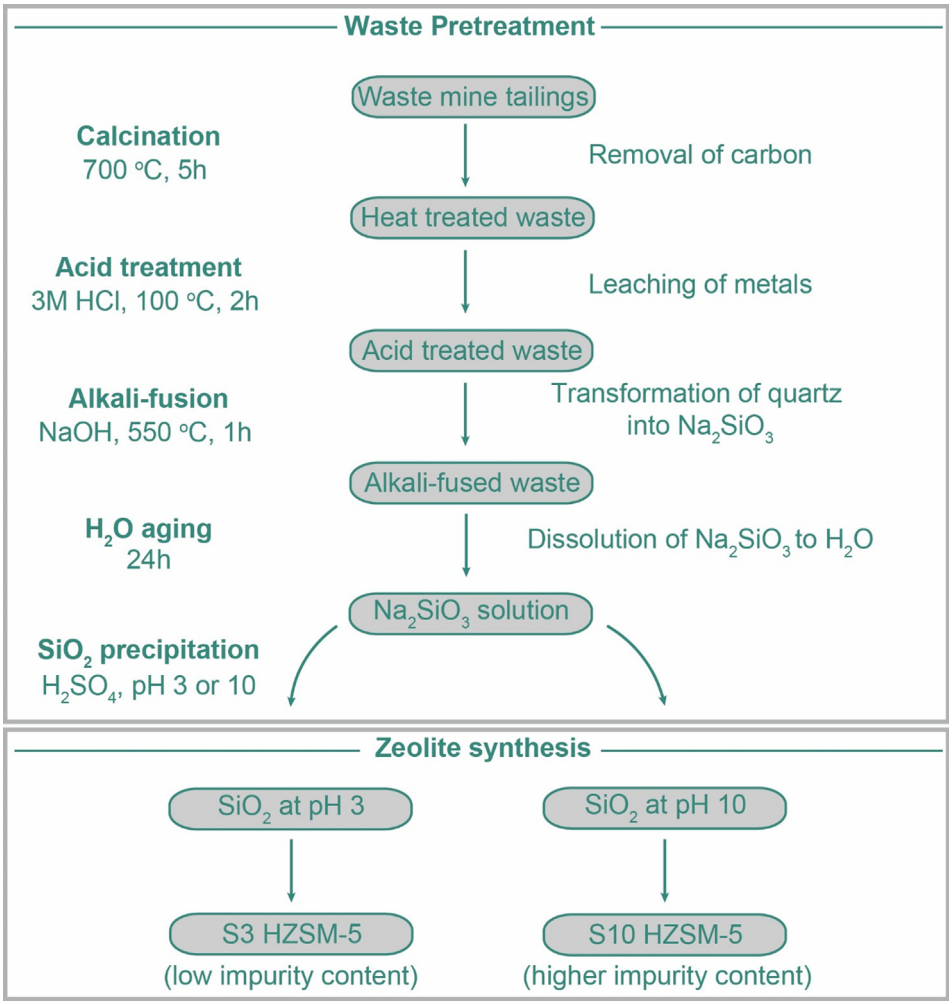

Scheme 1. Schematic representation of the synthesis of waste-derived zeolites. Illustration step-by-step of the synthesis of waste-derived zeolites ZSM-5 using waste flotation tailings from primary Cu production.

for 12 h in air and then calcined at 550 °C for 8 h under a flow of air to remove the template and to obtain NaZSM-5. The calcined NaZSM-5 material was then added to an aqueous solution of 30 mL 1 M NH_4NO_3 at 80 °C for 2.5 h. This procedure was repeated twice to make sure that the ion exchange of Na^+ for NH_4^+ was successful. The solid was separated from the supernatant, washed with H_2O and then dried at 60 °C for 12 h and calcined at 550 °C under a flow of air for 4 h in order to obtain the proton form of the zeolite ZSM-5 (further denoted as HZSM-5).

2.2. Materials characterization

The chemical composition of the materials made was determined by Inductively Coupled Plasma-Optical Emission Spectroscopy (ICP-OES) using a SPECTRO CIROS^{CCD} instrument of SPECTRO Analytical Instruments. This was done after bringing the solids in solution with aqua regia and lithium borate. The chemical composition of the waste flotation tailings was measured by X-ray Fluorescence (XRF) using a Thermo ARL 9400 sequential XRF instrument. Ar and N_2 physisorption measurements of the solids were performed using a Micromeritics TriStar 3000 instrument operating at −196 °C. Before performing the measurements, the samples were dried for 15 h at 300 °C under a N_2 flow. The morphology of the samples was determined by scanning electron microscopy (SEM) using a FEI Helios Nanolab G3 instrument. Prior to sample analysis, they were coated with a layer of Pt to increase their conductivity. X-ray diffraction (XRD) patterns of the materials were measured on a Bruker D2 X-ray powder diffractometer equipped with a Co Kα X-ray tube (λ = 1.7902 Å). Temperature-programmed desorption of ammonia (NH_3-TPD) was performed using a Micromeritics AutoChemII 2920 equipped with a thermal conductivity detector (TCD). Fourier transform-infrared (FT-IR) spectroscopy of adsorbed pyridine and carbon monoxide as probe molecules was carried out to probe the acid sites. FT-IR spectra were measured with a Bruker Vertex 70v spectrometer in the spectral range of 4000–1000 cm^{-1}. Experimental details of these measurements were described elsewhere [21,22]. Diffuse reflectance spectroscopy (DRS) in the UV–Vis–NIR region was performed using a Varian Cary 500 UV–vis–NIR spectrometer equipped with a DRS accessory to allow collection in diffuse reflectance mode against a pure white reference Teflon standard. X-band electron paramagnetic resonance (EPR) measurements were carried out with a Bruker EMX plus instrument at various temperatures with a 0.25 mT amplitude and 100 kHz modulation frequency. ~80 mg of sample was placed in a 4 mm diameter quartz tube and EPR spectra were recorded in the range 0–6000 Gauss.

2.3. Materials testing

Catalytic testing of the materials made was performed in a quartz fixed-bed rectangular reactor (ID = 6 mm × 3 mm) using ~69 mg of catalyst using a weight hourly space velocity (WHSV)

of 8 h^{-1} at 350 °C. A He flow with a methanol saturation of *ca.* 15% was obtained by flowing He as carrier gas through a saturator containing methanol at 21 °C. *Operando* UV–Vis DRS spectra were recorded using an AvaSpec 2048L spectrometer via a high-temperature UV–Vis optical fiber probe. Online analysis of methanol as reactant and the various reaction products made was performed using an Interscience Compact gas chromatograph (GC). Details of the catalytic set-up has been described elsewhere [22,23].

3. Results and discussion

3.1. Understanding the nature of the waste stream and the origin of impurities

Researchers have been using different types of waste streams as precursors for zeolite synthesis [7]. Pretreatment steps are usually necessary before waste materials can be used for the synthesis of zeolites as waste can contain various metal oxides as impurities. However, the pretreatment steps chosen, in each case, differ. In this study, waste mine flotation tailings are used as precursor for the synthesis of zeolite ZSM-5. SEM and N_2 physisorption provide information on the crystal morphology, while XRD gives insight into the minerals present and X-ray fluorescence (XRF) reveals the elemental composition of the waste material.

Scanning electron microscopy (SEM) images from the starting waste material (Fig. 1a) illustrated a non-porous material with compact morphology, as confirmed by N_2 physisorption since no specific surface area was detected. As can be observed in Fig. 1b, the XRF results for the waste mine flotation tailings showed that the sample mainly consists of silicon dioxide (SiO_2, i.e., 51.3%) in addition to calcium oxide (CaO, i.e., 16.1%), magnesium oxide (MgO, i.e., 10.9%), iron oxide (Fe_2O_3, i.e., 3.7%), aluminum oxide (Al_2O_3, i.e., 2.9%), sulfur (S, i.e., 1.6%), carbonaceous species and some moisture. These can be burned in a loss on ignition test (LOI, i.e., 13.53%). XRD confirms that quartz (SiO_2, red) is the main phase, as shown in Fig. 1c. In addition, dolomite ($CaMg(CO_3)_2$, blue), calcite ($CaCO_3$, green), clinochlore ($(Mg,Fe^{2+})_5Al(Si_3Al)O_{10}(OH)_8$, yellow), phlogopite ($KMg_3(AlSi_3O_{10})(OH)_2$, pink) and actinolite ($Ca_2(Mg_{4.5-2.5}Fe^{2+}_{0.5-2.5})Si_8O_{22}(OH)_2$, dark yellow) were also detected. The presence of calcium, magnesium and iron, as revealed by XRF, as well as quartz, as identified by XRD, can be problematic during zeolite synthesis. For example, iron competes with aluminum in the formation of the zeolite framework, thereby affecting its acidity and catalytic activity, while quartz as very dense phase is difficult to transform into a porous zeolite phase. Furthermore, elements, such as calcium and magnesium, have to be removed before starting the synthesis procedure as they may affect the acidic properties of the end material.

A schematic representation of zeolite synthesis, including the pretreatment step of the waste flotation tailings, is presented in Scheme 1. First, a calcination step is performed to remove the carbon deposits from the sample. Subsequently, an acid treatment is applied in order to remove the majority of the metal oxides, such as CaO, MgO and Fe_2O_3. Aiming for a greener synthesis approach, a calcination step is introduced to minimize the acid consumption during the acid treatment step since carbonates can react with the acid. An alkali-fusion step, in which the acid-treated waste was mixed with fine powder of sodium hydroxide (NaOH) at 550 °C for 1 h, was applied in order to produce sodium silicate (Na_2SiO_3). Sodium silicate is easily soluble in water. As a result, the alkali-fusion step helps with upgrading the inactive and stable quartz phase. In a next step, silica (SiO_2) is precipitated, using the Na_2SiO_3 aqueous solution, at two different pH values, namely at pH = 3 and pH = 10. By altering the pH during SiO_2 precipitation, the formation

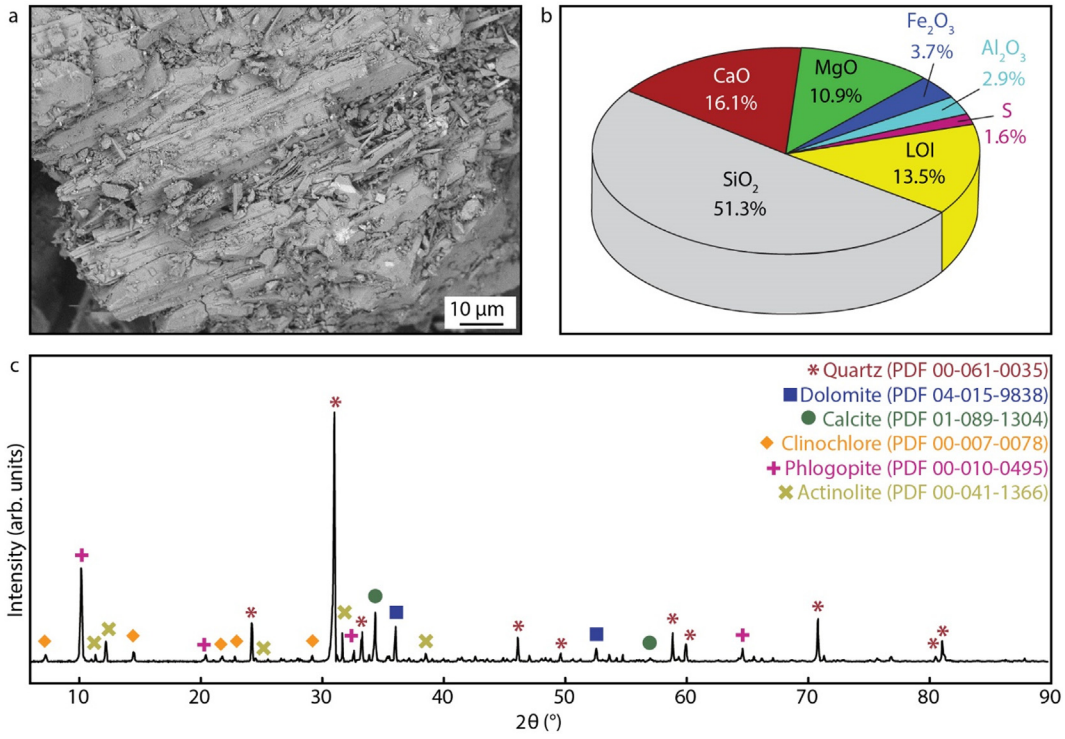

Fig. 1. Physicochemical characterization of the waste mine flotation tailings used in this study. a) Scanning electron microscopy (SEM) image obtained for the sample b) X-ray fluorescence (XRF) analysis showing the chemical composition consisting mainly of SiO_2 (gray) as well as CaO, MgO, Fe_2O_3, Al_2O_3, sulfur and some carbonaceous species (red, green, blue, cyan, pink and yellow, respectively) c) X-ray diffraction (XRD) powder pattern, including the XRD lines of quartz (red), dolomite (blue), calcite (green), clinochlore (yellow), phlogopite (pink) and actinolite (dark yellow) as reference compounds.

of metal hydroxides can be controlled in order to vary the impurity level and determine the effect of impurities on the catalytic performance of the waste-derived zeolites. The solubility of divalent metals, such as Mg, Ca and Fe^{2+}, decreases at pH higher than 7 and thereby increases precipitation. In contrast, at lower pH, the divalent metals are soluble, while Fe^{3+} and Al^{3+} appear to precipitate [24,25]. Consequently, SiO_2 precipitated at pH = 3 (i.e., sample S3) has a low amount of impurities, while SiO_2 precipitated at pH = 10 (i.e., sample S10) has a higher amount of impurities. The silica samples S3 and S10 have been used as precursors for synthesis of zeolites denoted S3 HZSM-5 and S10 ZSM-5.

3.2. Impurities effect on physicochemical properties of waste-derived zeolites

The prepared zeolites were characterized and compared to a commercial zeolite ZSM-5 sample and a zeolite ZSM-5 synthesized using fumed silica as precursor (further denoted as Com HZSM-5 and FS HZSM-5, accordingly). Inductively coupled plasma-optical emission spectroscopy (ICP-OES) analysis has been used to obtain the elemental composition of the zeolite-based materials under study, and the results are summarized in Table 1.

Com HZSM-5 and FS HZSM-5 appear to have a low amount of impurities (i.e., Ca, Fe, Mg and Na). As expected, the sample prepared with SiO_2 obtained at pH 10 shows a much higher amount of impurities compared to the sample prepared with SiO_2 obtained at pH 3, underlining the correlation of the pH during the SiO_2 precipitation step with the content of impurities. Even though the pretreatment removes high amounts of impurities, the procedure is not 100% effective since the impurity levels of S3 HZSM-5 is still higher than the commercial zeolite and zeolite prepared using fumed silica. In addition, Na is also not completely removed after the alkali-fusion and dissolution/precipitation step of the pretreatment, even after zeolite synthesis and subsequent ion exchange. This can be explained by the excess of NaOH used during the alkali-fusion step in order to transform quartz into Na_2SiO_3.

As shown by the ICP-OES analysis, the amount of impurities in waste-derived zeolites can be regulated by adjusting the pretreatment steps of the waste flotation tailings before using it for the synthesis of zeolite materials. Further characterization of the materials obtained revealed the effect of these impurities on their physicochemical properties.

The SEM images, shown in Fig. 2a-d, of the waste-derived zeolites as well as the references ZSM-5 materials, revealed the differences in morphology between commercial, zeolite prepared from high purity fumed silica and waste-derived zeolite ZSM-5. The commercial zeolite consists of typical coffin-shape crystals with the size of 1–5 μm along the *c*-axis. In contrast, FS sample consists of spherical agglomerate, with the size of 0.4–2.5 μm, of smaller crystals. Regarding the waste-derived samples, S3 HZSM-5 consists of spherical agglomerates with the size of 0.5–5 μm, which consist of smaller cube-like crystals, while S10 HZSM-5 appears to be spherical agglomerates with the size of 2–10 μm, which consist of smaller sheet-like crystals. The differences observed in the morphology between the waste-derived samples can be attributed to the higher content of Na, Ca, Mg and Fe cations. These cations could act as inorganic template species and framework-charge compensating cations, which would explain the different morphologies of zeolite ZSM-5 [26]. The aforementioned phenomena are in line with observations that the crystal size and zeolite crystallization processes can be affected by replacing Na cations, in the zeolite synthesis mixture, with other alkali metals [27–29].

Fig. 2e-f show the results obtained from Ar physisorption for the four zeolite samples under study. Sorption measurements (Fig. 2f) showed that the isotherm of Com HZSM-5 were type I, which is characteristic for microporous materials with relatively small external surfaces, while FS HZSM-5, S3 HZSM-5 and S10 HZSM-5 exhibited a hysteresis loop, H4, which is a combination of types I and II isotherms and they are usually found in agglomeration of zeolite crystals and/or mesoporous zeolites [30].

As shown in Fig. 2e, all samples show hierarchical porosity. More specifically, the Com HZSM-5, FS HZSM-5 and S3 HZSM-5 exhibit a bimodal pore size distribution with the first peak to appear in the range < 1 nm and the second peak centered at ~3 nm. For sample S10 HZSM-5 additional porosity is observed with a pore size of ~4.5 nm. As shown in Fig. 2d, S10 HZSM-5 consists of agglomerates of sheet-like ZSM-5 crystals. The mesopores formed in this sample could be attributed to spaces between sheet-like MFI crystals, which form larger agglomerates [31]. In Fig. 2f, the specific surface area (SSA) of the four samples are presented. FS sample showed the highest SSA. The two waste-derived samples showed lower SSA compared to FS sample which can be attributed to the increased amount of impurities in the waste-derived samples as residual impurities can block the pores of zeolites. In addition, the waste-derived samples exhibited higher SSA compared to the commercial zeolite ZSM-5. The pore system is crucial for the catalytic performance during for example the MTH process as it can influence the catalyst selectivity as well as its deactivation [32]. Recent studies show that the presence of additional mesopores and macropores provides to zeolites an increased lifetime relative to microporous materials [32–34]. Understanding the pore structure of waste-derived ZSM-5 zeolites can be the key to explain their catalytic behavior.

In order to further investigate the effect of the impurities on the structure and properties of the zeolite materials, X-ray diffraction (XRD) and Fourier transform-infrared (FT-IR) spectroscopy are performed and the results are summarized in Fig. 3.

Fig. 3a shows that the crystal phase of all four samples is characteristic of an MFI zeolite. It can be observed that the zeolite prepared using fumed silica and the waste-derived zeolites showed XRD patterns of lower intensity, while the higher full width at half maximum (FWHM) implies a lower crystallinity compared to the commercial zeolite ZSM-5. This can be explained by the fact that these samples were synthesized using fumed silica or amorphous silica (SiO_2) as precursor extracted from the waste and not from sodium silicate ($NaSi_2O_3$) or tetraethyl orthosilicate (TEOS), which are typically used as silicon precursors [35].

The FT-IR spectra of all four zeolites ZSM-5 are presented in Fig. 3b-c. All the samples show FT-IR peaks at characteristic wavelengths in two specific regions, i.e. the 1600–2000 cm^{-1} spectral

Table 1
Overview of the chemical composition of the waste-derived zeolites, as well as the reference ZSM-5 material. ICP-OES analysis of commercial zeolite ZSM-5 (denoted as Com HZSM-5), zeolite ZSM-5 prepared using fumed silica (denoted as FS HZSM-5) and waste-derived zeolites ZSM-5 obtained at pH 3 (denoted as S3 HZSM-5) and 10 (denoted as S10 HZSM-5).

	Si (wt.%)	Al (wt.%)	Ca (wt.%)	Fe (wt.%)	Mg (wt.%)	Na (wt.%)
Com HZSM-5	33.7	1.92	0.065	0.010	0.040	0.010
FS HZSM-5	34.7	2.07	0.037	0.003	0.004	0.005
S3 HZSM-5	30.24	2.27	0.073	0.11	0.038	0.13
S10 HZSM-5	24.03	3.20	0.29	0.33	0.37	0.18

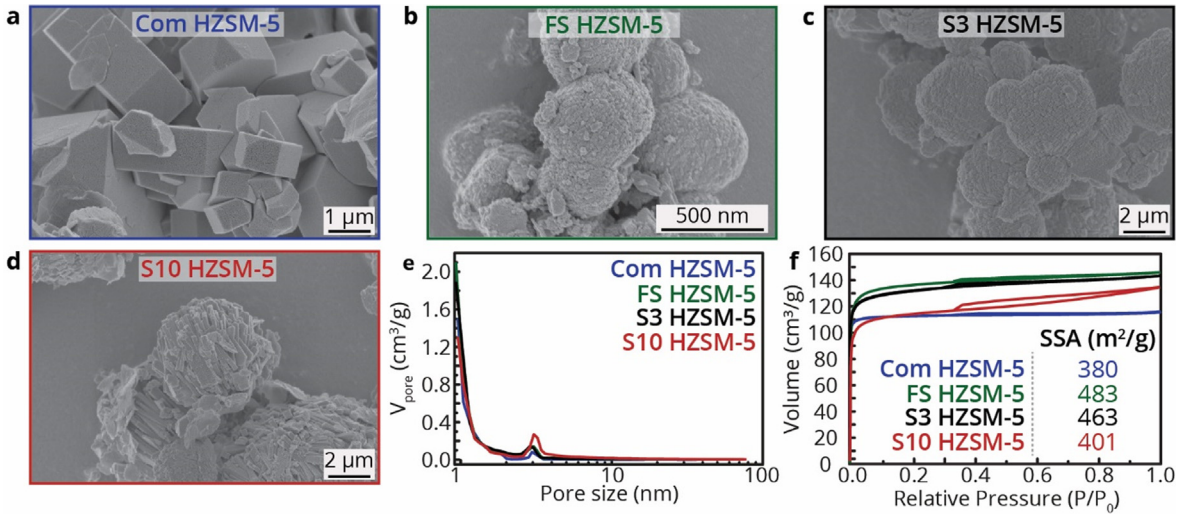

Fig. 2. Particle morphology and porosity of the waste-derived zeolites, as well as the reference ZSM-5 material. Scanning electron microscopy (SEM) images of a) commercial zeolite ZSM-5 (blue; denoted as com HZSM-5), b) zeolite ZSM-5 prepared using fumed silica (green; denoted as FS HZSM-5) and waste-derived zeolites ZSM-5, prepared c) at pH 3 (black; denoted as S3 HZSM-5) and d) at pH 10 (red; denoted as S10 HZSM-5) e) Pore volume distribution and e) isotherms and specific surface area (SSA) for the com HZSM-5, FS HZSM-5, S3 HZSM-5 and S10 HZSM-5 materials.

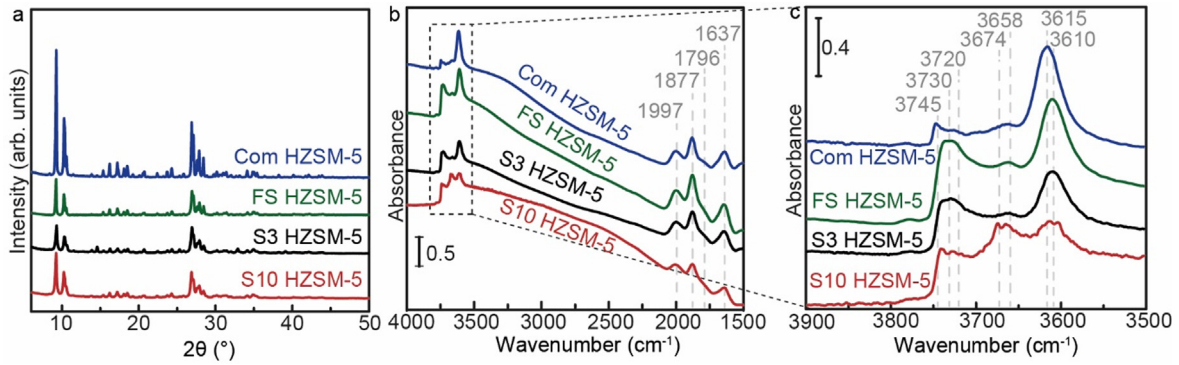

Fig. 3. Structural analysis of the waste-derived zeolites, as well as the reference ZSM-5 material, including their acidic properties. a) X-ray diffraction (XRD) patterns for com HZSM-5, FS HZSM-5, S3 HZSM-5 and S10 HZSM-5 (blue, green, black and red, respectively) b) FT-IR spectra for com HZSM-5, FS HZSM-5, S3 HZSM-5 and S10 HZSM-5 (blue, green, black and red, respectively) taken under vacuum after drying the materials for 2 h at 550 °C; and c) zoom-in of the –OH stretching region of the four samples.

window and the 3500–3800 cm^{-1} spectral window. The peaks, in the 1600–2000 cm^{-1} region can be attributed to overtones and combination bands of zeolite framework modes. In the second region, known as the –OH region, the commercial zeolite shows peaks centered at ~3615, ~ 3658, ~3745, ~ 3730 and ~3720 cm^{-1}. The vibration at ~3615 cm^{-1} is due to the acidic bridging Si(OH)Al groups (i.e., Brønsted acid sites, BAS), while the peak at ~3658 cm^{-1} is typical for extra-framework Al species. The three peaks at ~3745, ~ 3730 and ~3720 cm^{-1} are attributed to SiOH in external and mesopores surfaces, terminal SiOH or extra-framework SiO_2 and SiOH in defects [36,37]. Samples FS and S3 HZSM-5 show similar FT-IR peaks at the ~3610 and ~3658 cm^{-1} (BAS and extra-framework Al, accordingly) and a broader peak at ~3730 cm^{-1}. The latter can be attributed to the co-existence not only of terminal SiOH or extra-framework SiO_2 but also SiOH in external and mesopores surfaces (~3745 cm^{-1}) and SiOH in defects (~3720 cm^{-1}). The ratio of the intensities of the peaks at 3610 and 3730 cm^{-1}, for samples FS and S3, is lower than for com HZSM-5 indicating a lower amount of BAS and higher amount of silanol groups. Sample S10 HZSM-5 shows the same peaks at ~3610 and ~3730 cm^{-1} as sample FS and S3 HZSM-5, but also an extra peak at ~3674 cm^{-1}. According to characterization studies of Fe-exchanged zeolites, the latter FT-IR peak can be attributed to hydroxyl groups bonded to extra-framework Fe species [38]. These FT-IR vibrations can be assigned to the stretches of two hydroxyl groups, which are bonded to one Fe center [38]. These hydroxyl group are weakly acidic sites and created by the presence of Fe impurities, originating from the initial waste. This observation also proves that the control of the impurities during the pretreatment has a direct influence on the physicochemical properties of the waste-derived zeolite materials. When the impurity content increases, more Fe species are incorporated in the zeolite structure and hence more weak acid sites are formed. As reported in Table 1, our waste-derived zeolites have higher amounts of Fe. In numerous literature studies, Fe-modified zeolites are used for improving the ammonia Selective Catalytic Reduction (NH_3-SCR) and MTH reactions [38–42]. In these studies, various characterization techniques have been used for the investigation of the nature of Fe(III) species and among them UV–Vis diffuse reflectance spectroscopy (DRS) and electron paramagnetic resonance (EPR) are most commonly used. Hence, also in our study, UV–Vis DRS and EPR are employed in order to better understand the nature of Fe species in the waste-derived zeolite ZSM-5 materials.

Fig. 4a shows the UV–Vis DRS data for sample S3 HZSM-5 with absorption maxima at ~210 nm and ~250 nm with a broad absorption shoulder towards ~400 nm. The absorption bands can be fitted

using 4 Gaussian curves centered at 210, 250, 305 and 350 nm. These fitted Gaussians correspond to the $Fe^{3+} \leftarrow O$ charge-transfer (CT) bands of the waste-derived samples. The two sub-bands at the high-energy range of the spectra (<300 nm, purple) are related to isolated Fe species with a tetrahedral or higher coordination environment. Between 300 and 400 nm, low intensity broad bands (orange) arise due to the presence of octahedral Fe^{3+} ions in small oligonuclear clusters of the type Fe_xO_y [41].

Sample S10 HZSM-5 shows a similar UV–Vis DRS spectrum, as shown in Fig. 4b. However, the absorption shoulder at lower energies (>350 nm) is more pronounced. When fitting the UV–Vis DRS spectrum, Gaussian curves are obtained, which are centered at the same energies as compared to sample S3 HZSM-5 (purple and orange) in addition to two additional Gaussian curves (cyan). The latter Gaussian curves centered at ~450 and ~510 nm are attributed to larger Fe_2O_3 clusters [41]. Although they are clearly visible in the UV–Vis DRS spectra, the dominant species remain isolated Fe^{3+} and oligomeric Fe_xO_y species based on the relative intensities of the absorption bands [41]. Comparing the two waste-derived samples, it can be concluded that formation of larger Fe_2O_3 clusters occurs by increasing the impurities content. This phenomenon can influence the acidity of the samples since the presence of Fe species can block certain acid sites of the zeolites or even create Lewis acid sites, as observed in Fig. 3.

The EPR spectra of samples S3 HZSM-5 and S10 HZSM-5 are shown in Fig. 4c-d, respectively. These EPR spectra were taken from room temperature down to 99 K for both samples. Sample S3 HZSM-5 showed three different signals at g-values of 2, 2.6 and 4.3. The EPR signal at g = 4.3 is assigned to isolated Fe^{3+} species in tetrahedral coordination, which can be Fe species in the framework or extra-framework species in a zeolite [41,43]. The EPR signal at g = 2.6 can be assigned to Fe oxide or Fe hydroxyl species in the zeolite pores, while the EPR signal at g = 2 can be due to Fe^{3+} isolated species with high symmetry or Fe clusters in which Fe ions interactions are equal to the zero field splitting [41,43]. Sample S10 HZSM-5 shows similar EPR signals at g-values equal to 2 and 4.3, but not the EPR signal at g = 2.6. On top of that, an extra line at ~g = 6 can be observed, which is related to isolated Fe species with higher coordination numbers [41,43]. Regarding the g = 2 EPR signal, six weaker lines can be observed. These features can be assigned to the hyperfine-structure of paramagnetic Mn^{2+} species [44]. Indeed, ^{55}Mn has a nuclear spin (I) of 5/2, which will couple with the electron spin, leading to 6 sublevels. In addition, since ^{56}Fe is the most common isotope (92%) and has a spin of 0, this hyperfine structure cannot be due to the presence of Fe. Mn^{2+} species can originate from the initial waste flotation tailings and can be easily detected by EPR spectroscopy even in trace amounts [45]. In total, EPR spectroscopy on the waste-derived samples

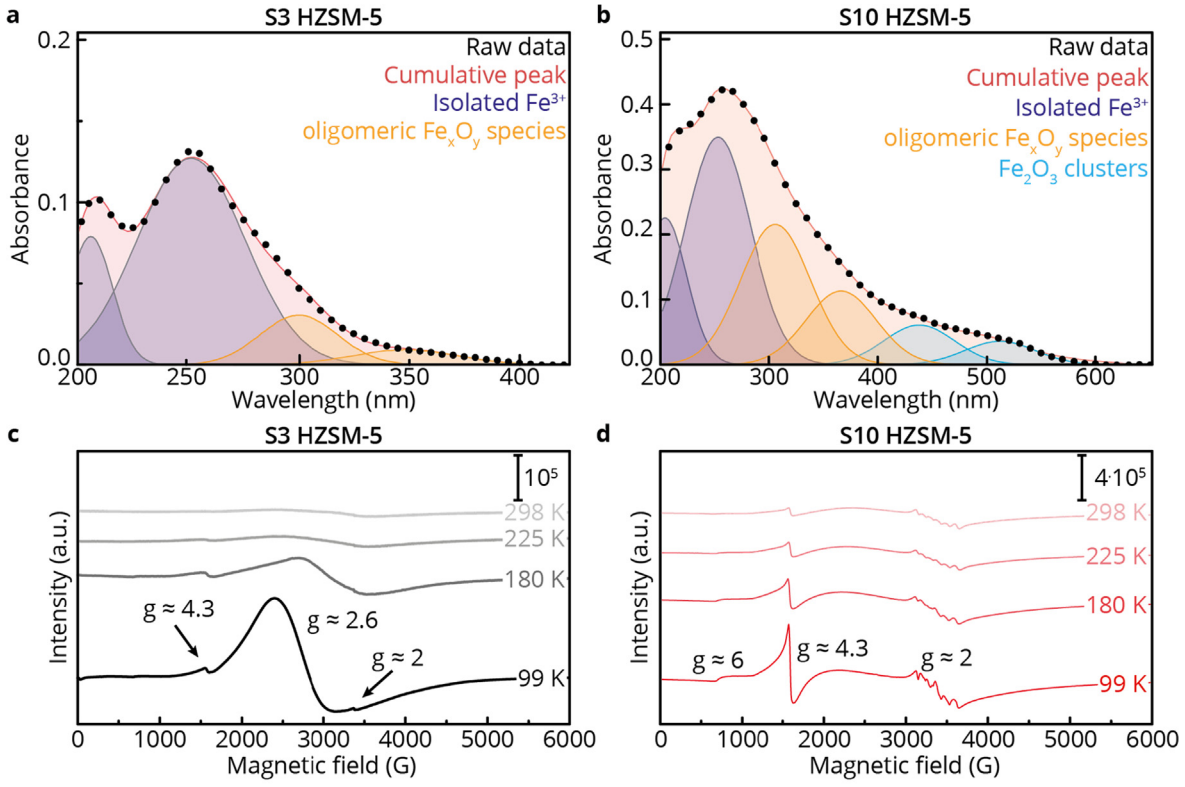

e

Sub-bands derived by fitting with Gaussians	λ = 205 nm	λ = 250 nm	λ = 305 nm	λ = 350 nm	λ = 440 nm	λ = 510 nm
S3 HZSM-5	15 %	45 %	35 %	5 %	0 %	0 %
S10 HZSM-5	9 %	39 %	26 %	14 %	7 %	5 %

Fig. 4. Spectroscopic identification of Fe species present in the waste-derived zeolites. UV–Vis diffuse reflectance spectra (DRS) for a) S3 HZSM-5 and b) and S10 HZSM-5, Electron paramagnetic resonance (EPR) spectra for c) S3 HZSM-5 and d) and S10 HZSM-5 and e) Percentage of the area from the deconvoluted absorption bands of the UV–Vis DRS data.

showed that the increase of the impurities content can affect the type of Fe species in the samples. On top of that, it revealed the presence on Mn^{2+} species for sample S10.

It is already established in the literature that the presence of cations, such as Ca, Mg and Fe, during zeolite synthesis or as zeolite post-modification can influence the overall acidity and as a result affect their catalytic performance in e.g. the MTH process [22,46,47]. As a consequence, it is expected that the presence of impurities influences the acid sites present in the waste-derived zeolites. In order to fully understand the impact of these impurities on the acidic properties of the waste-derived zeolite materials, Ammonia Temperature Programmed Desorption (NH_3-TPD) was performed to determine the total amount of acid sites and also gather information on the strength of the different acid sites present. In addition, absorption of pyridine followed by FT-IR spectroscopy (further denoted as Py-FT-IR) was performed to differentiate between Brønsted acid sites (BAS) and Lewis acid sites (LAS). Moreover, CO adsorption followed by FT-IR spectroscopy (further denoted as CO-FT-IR) has been used to investigate the different hydroxyl groups present in the waste-derived zeolites as well as in the commercial zeolite.

From the NH_3-TPD analysis data, shown in Fig. 5a, the strength of the acid sites could be determined as well as the total amount of acid sites of the samples under study. For the Com HZSM-5 and FS HZSM-5, two major peaks were recorded centered at ~250 °C and ~445 °C. The peak at ~250 °C can be attributed to weak acid sites, and the peak at ~445 °C can be assigned to strong acid sites [21,48,49]. Sample S3 HZSM-5 exhibits a lower amount of total acid sites, namely 0.93 mmol/g (this value has to be compared to 1.11 mmol/g for the commercial ZSM-5 sample and to 1.01 for the zeolite ZSM-5 synthesized from fumed silica), which can be explained by the presence of impurities, such as FeO_x, MgO, CaO and Na_2O. These impurities can block the acid sites of the waste-derived zeolite materials. As aforementioned in Fig. 3c, the peak corresponding to Si(OH)Al bridging hydroxyl groups (i.e. BAS) is more pronounced in com HZSM-5 than in S3 HZSM-5. Sample S10 showed an even lower amount of acid sites, which equals 0.75 mmol/g, which can be explained by the even higher amount of impurities. Also, in this case, a decrease in BAS is observed. This can be explained by the higher amount of extra-framework Fe (in addition to FeO_x, CaO, MgO and Na_2O), which can block the strong acid sites. The increased number of intermediate acid sites in sample S10 HZSM-5 are corroborated by our previous findings that by increasing the impurities content and therefore the iron content, weakly acidic hydroxyl groups are formed, which are bonded to Fe centers (Fig. 3c). It is worth mentioning that there is a seemingly inconsistency between Si/Al ratio and the BAS of the samples. From Table 1, it can be calculated that the atomic Si/Al ratio for the commercial, FS, S3 and S10 samples are 17.5, 16.7, 13.3 and 7.2 accordingly. It would be expected that the BAS will increase by decreasing the Si/Al ratio (increase of Al content). However, the opposite phenomenon is observed which can be attributed to the fact that the higher Al content does not translate to Al incorporated in the zeolite framework as well as the increased impurities levels for the case of the waste-derived zeolites ZSM-5.

Fig. 5b shows Py-FT-IR spectra of the four samples under study, in which the peak at ~1445 cm^{-1} can be assigned to the presence of LAS, while the peak at ~1545 cm^{-1} can be assigned to BAS [21]. Compared to Com HZSM-5 and FS HZSM-5, samples S3 HZSM-5 and S10 HZSM-5 show a decrease in the amount of BAS, while sample S10 HZSM-5 shows an increase in LAS. The decreased amount of BAS for the waste-derived zeolite samples can be explained by the presence of impurities originated from the initial waste, while the increased amount of LAS for sample S10 HZSM-5 can be explained by the presence of small oligomeric Fe_xO_y moieties as well as extended Fe_2O_3-like clusters, which can act as LAS. These findings are in line with the above-mentioned NH_3-TPD data, which show a change in the presence of strong acid sites, as well as the total acidity.

The CO-FT-IR experiments, shown in Fig. 5c, revealed the nature of the different –OH groups present in the zeolite-derived materials. All samples show similar FT-IR spectra after CO adsorption with absorption peaks present at ~2175, 2158 and 2138 cm^{-1}, which correspond to BAS, silanol groups and physisorbed CO,

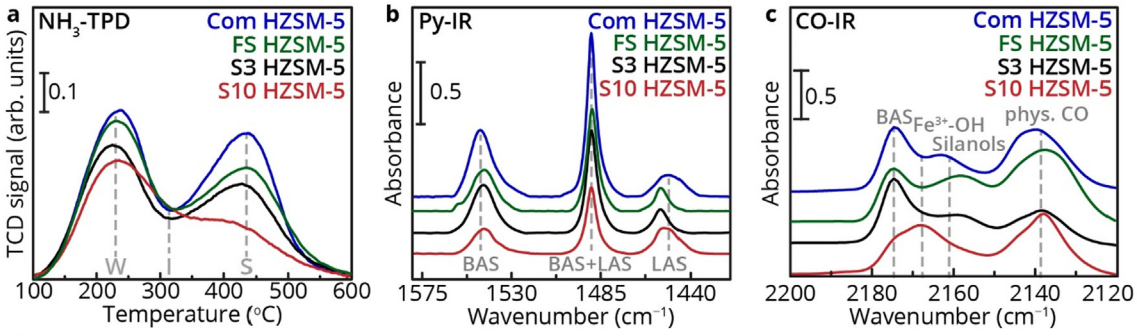

d

	Acid sites by NH_3-TPD (mmol/g)				Acid sites by Py-IR (mmol/g)		
	weak	intermediate	strong	total	BAS	LAS	BAS/LAS
Com HZSM-5	0.56	0.10	0.45	1.11	0.53	0.10	5.3
FS HZSM-5	0.54	0.09	0.38	1.01	0.51	0.11	4.6
S3 HZSM-5	0.50	0.08	0.35	0.93	0.39	0.08	4.9
S10 HZSM-5	0.44	0.13	0.18	0.75	0.30	0.22	0.76

Fig. 5. Investigation of the acidic properties of the waste-derived zeolites, as well as the reference ZSM-5 material. a) NH_3-TPD (temperature programmed desorption) analysis of S3 HZSM-5 (black), S10 HZSM-5 (red), com HZSM-5 (blue) and FS HZSM-5 (green). b) Py-FT-IR (Fourier-transform infrared) spectra measured at 150 °C of S3 HZSM-5 (black), S10 HZSM-5 (red), com HZSM-5 (blue) and FS HZSM-5 (green). c) CO-FT-IR spectra of S3 HZSM-5 (black), S10 HZSM-5 (red), com HZSM-5 (blue) and FS HZSM-5 (green). d) Table containing the amount of different acid sites (labeled as weak, intermediate and strong), as determined and calculated from the NH_3-TPD data, while the amount of Brönsted acid sites (BAS), Lewis acid sites (LAS) and their ratio, are determined and calculated using the Py-FT-IR data.

respectively [22]. However, the FT-IR spectrum of sample S10 HZSM-5 has an extra absorption at ~2168 cm^{-1}. The presence of Fe, as shown by FT-IR, UV–Vis DRS and EPR (Figs. 3 and 4), explains the presence of the 2168 cm^{-1} absorption, which can be attributed to –OH groups related to isolated Fe^{3+} species.

3.3. Linking physicochemical properties with catalytic performances

In order to investigate the effect of the physicochemical properties of the waste-derived zeolites on their catalytic performance, the activity and selectivity of the zeolites in the MTH reaction were evaluated. Fig. 6 displays the catalytic conversion and the yield of the different reaction products (i.e., ethylene, propylene, isobutylene, C5 paraffins, and C5 olefins) formed during the MTH reaction performed at 350 °C for 900 min using a weight hourly space velocity (WHSV) of 8 h^{-1}.

The Com HZSM-5 and FS HZSM-5 show a methanol conversion close to 100%, which starts to decrease around ~300 min. The deactivation can be attributed to the accumulation of non-active hydrocarbon species in the zeolite pores, due to the high amount of BAS [50,51]. The waste-derived zeolite samples show high values of methanol conversion (>80%). It can be observed that sample S10 HZSM-5, with the higher amount of impurities, also shows a slightly lower initial methanol conversion, which can be attributed to the lower amount of acid sites. After a decrease in the first 200 min of time-on-stream (TOS) the waste-derived catalyst stabilizes its catalytic performance with a methanol conversion of ~87%, while sample S3 HZSM-5 exhibits a higher conversion (>96%) for at least 900 min. Knowing that S3 HZSM-5 and S10 HZSM-5 contained respectively more and less BAS, it is expected that sample S3 HZSM-5 would deactivate faster. However, sample S10 HZSM-5 showed an initially faster deactivation and a decrease in methanol conversion, which can be attributed to the difference in the crystal morphology and size. As shown in Fig. 2b-c, sample S10 HZSM-5 shows spherical agglomerates with sizes of ~2–10 μm, which consist of smaller sheet-like HZSM-5 crystals, while sample S3 HZSM-5 shows agglomerates with the size of 0.5–5 μm which consist of smaller cube-like HZSM-5 crystals. According to literature, it is known that crystal morphology and size are linked to the lifetime of a MTH catalyst and that the lifetime of the zeolite is increased by decreasing the crystal size [52].

Interestingly, Com HZSM-5, FS HZSM-5 and S3 HZSM-5 showed similar yields of ethylene, propylene, *iso*-butylene, C_5 paraffins and C_5 olefins for the first 400 min of reaction. However, it can be observed that S10 sample exhibited higher yield of propylene initially (i.e., the first 500 min). The higher yield of propylene for sample S10 as well as the higher yields of *iso*-butylene, C_5 paraffins and olefins for samples Com, FS and S3 can be explained by the fact that hydride transfer reactions form C_1-C_5 paraffins and aromatics are promoted by Brønsted acid sites [50]. Thus, an enhanced contribution of the olefinic cycle to the overall catalytic performance and therefore propylene production is observed for S10 sample due to lower amount of BAS. Moreover, S10 HZSM-5 not only exhibits higher yields of propylene, but also higher yields of ethylene, which is in contrast with the decrease of BAS. However, the S10 HZSM-5 sample shows a higher amount of LAS. Recent studies have shown the importance of LAS in the MTH reaction and that reaction intermediates from the hydrocarbon pool (HCP), which are formed on LAS, are less reactive and inhibit chain reactions related to aromatic moieties [46]. Thus, S10 HZSM-5 exhibited a higher ethylene yield due to the lower reactivity of the aromatic HCP intermediates to form polyaromatics species. Summarizing, it is clear that the control over the impurities content in the waste-derived zeolite materials have an impact on their physicochemical catalytic properties.

3.4. Operando spectroscopy of waste-derived zeolites

Operando UV–Vis DRS has been used as a spectroscopic technique for the identification of zeolite-trapped hydrocarbon species formed during the MTH process [52,53]. UV–Vis DRS can distinguish between carbocationic hydrocarbon pool species, their neutral analogues as well as deactivating carbon deposits [53–55]. In this study, *operando* UV–Vis DRS was used for understanding the effect of impurities in waste-derived zeolite ZSM-5 materials and how these impurities may alter the MTH mechanism. Multiple

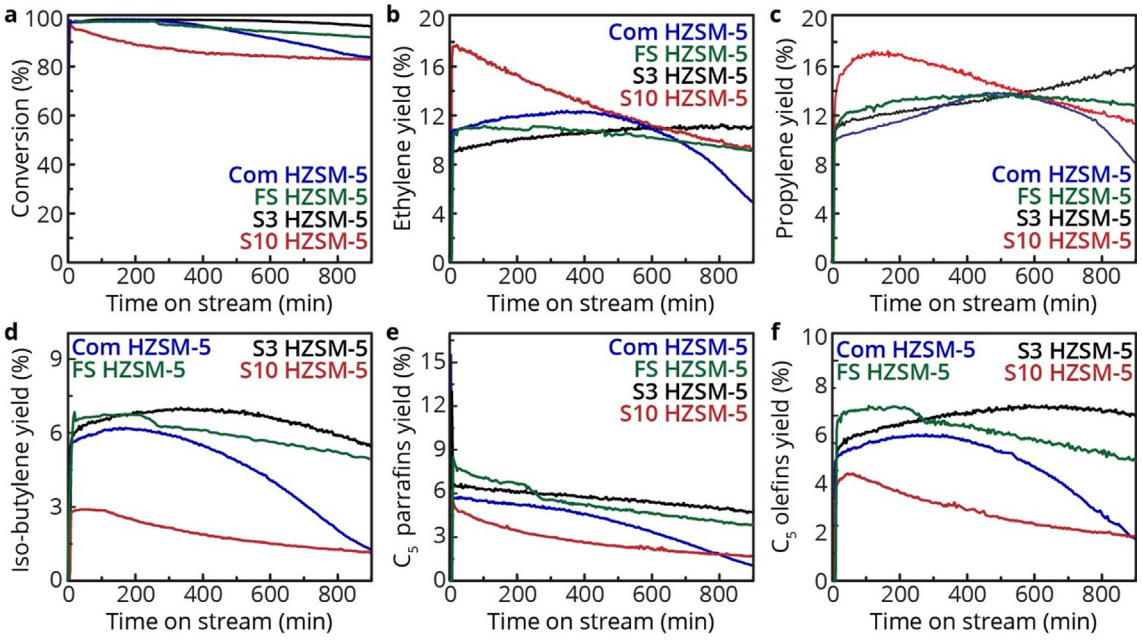

Fig. 6. Catalytic behavior in the Methanol-to-Hydrocarbons (MTH) reaction. Activity and selectivity of com HZSM-5 (blue), FS HZSM-5 (green), S3 HZSM-5 (black) and S10 HZSM-5 (red) zeolites vs. time for the MTH reaction conducted at 350 °C with a weight hourly space velocity (WHSV) of 8 h^{-1}. a) Total conversion, b) ethylene yield, c) propylene yield, d) *iso*-butylene yield, e) C_5 paraffins yield and f) C_5 olefins yield.

absorption bands in the UV–Vis DRS data were observed between 250 nm and 1000 nm, as illustrated in Fig. 7. All four samples show absorption bands at ~285 nm, ~ 420 nm and > 500 nm. In addition, Com HZSM-5 also shows an absorption band at ~335 nm, FS HZS-5 and S3 HZSM-5 show an additional band at ~364 nm, while S10 HZSM-5 shows extra absorption bands at ~352 nm and ~378 nm. These absorption bands can be attributed to neutral benzene/cyclopentadienyl (i.e., 285 nm), mono- and dienylic cations (i.e., 335 nm, 352 nm and 364 nm), highly methylated areniums (i.e., 378 nm), naphthalene and/or anthracene (i.e., 420 nm) and, finally methylated polyareniums ions/ highly conjugated polyenes (>500 nm)[23,46,55–58].

It is evident from Fig. 7 that Com HZSM-5, FS HZSM-5 and S3 HZSM-5 show higher amounts of aromatic hydrocarbon species, which is related to the higher amount of Brønsted acid sites present in these catalyst, which promote hydride transfer reactions. Furthermore, aromatic hydrocarbon species could take part in the aromatic cycle in which methylation and dehydration reactions lead to the formation of intermediate methylated aromatics. This is in line with the higher intensity of the absorption bands at ~285 nm, ~ 364 nm and ~420 nm, which is also shown in Fig. 7e by plotting the 285 nm band intensity versus TOS. In contrast, sample S10 HZSM-5 showed a lower formation of the HCP pool species (as evidenced in Fig. 7e-f) due to the lower amount of BAS. Interestingly, deactivation hydrocarbon species can be observed in all samples, as represented by absorption bands at wavelengths above 500 nm. Fig. 7g-h illustrate the absorption intensities of deactivation species at 500 nm, attributed to methylated poly-arenium ions, and at 900 nm, attributed to highly conjugated polyenes versus TOS. The sample synthesized from fumed silica and the two waste-derived zeolite samples showed a similar formation of methylated poly-arenium ions compared to the commercial zeolite sample, but a much higher amount of highly conjugated polyenes, most likely due to the different morphology between the waste-derived and commercial zeolite samples. As Com HZSM-5 has a morphology of cube-like ZSM-5 crystals between 1 and 5 µm, while the other three zeolite samples have spherical agglomerates of smaller crystals, there is a higher probability to form highly conjugated polyenes.

The results from Fig. 7 show that the waste-derived zeolite materials can compete with Com HZSM-5 and FS HZSM-5 when considering both catalyst activity and stability. The S3 HZSM-5 sample shows similar initial methanol conversion compared to Com HZSM-5 and FS HZSM-5 while S3 sample has a higher activity after the initial 300 min. Although the initial activity of the S10 HZSM-5 sample is lower compared to Com HZSM-5, the catalyst stability with increasing TOS is better, resulting in a similar catalytic activity after a TOS of 900 min. Even though the waste-derived zeolite samples show a similar or higher catalyst stability, the amount of deactivating hydrocarbon species observed with UV–Vis DRS is higher. Although this seems counter-intuitive, it is likely that the higher amount of deactivating hydrocarbon species is overcome by the larger intra-crystal space and pore sizes of the waste-derived samples, which help to prevent catalyst deactivation [59].

4. Conclusions

The influence of impurities in waste-derived zeolite materials was studied for the methanol-to-hydrocarbons (MTH) reaction. ZSM-5 zeolite-based materials were synthesized using waste from primary copper production as silicon precursor. Pretreatment of the waste allowed for the control of the impurity content in the final zeolite material. To investigate the effects of these impurities on the zeolite materials and their physicochemical properties and catalytic performances, samples with different impurity contents, i.e., Fe, Mg, Ca, Na, have been prepared. It was for example found that the sample with a low amount of impurities showed agglomerates of small cube-like zeolite ZSM-5 crystals, while the sample with higher impurities appeared to consist of agglomerates of larger sheet-like zeolite ZSM-5 crystals. FT-IR spectroscopy studies revealed the presence of weakly acidic hydroxyl groups associated with the Fe centers for the sample with the highest Fe content. Moreover, UV–Vis DRS and EPR revealed the existence of Fe species, which can alter the ratio of Brönsted acid sites (BAS)-to-Lewis acid sites (LAS). NH_3-TPD and FT-IR spectroscopy with pyridine and CO as probe molecules were used to assess the effect of these impurities on the acidic properties of the materials. The increase in the impurities content clearly has an impact on the zeolite acidity as it resulted in a decrease in the number of BAS, while the number of LAS increased. The catalytic performance of the

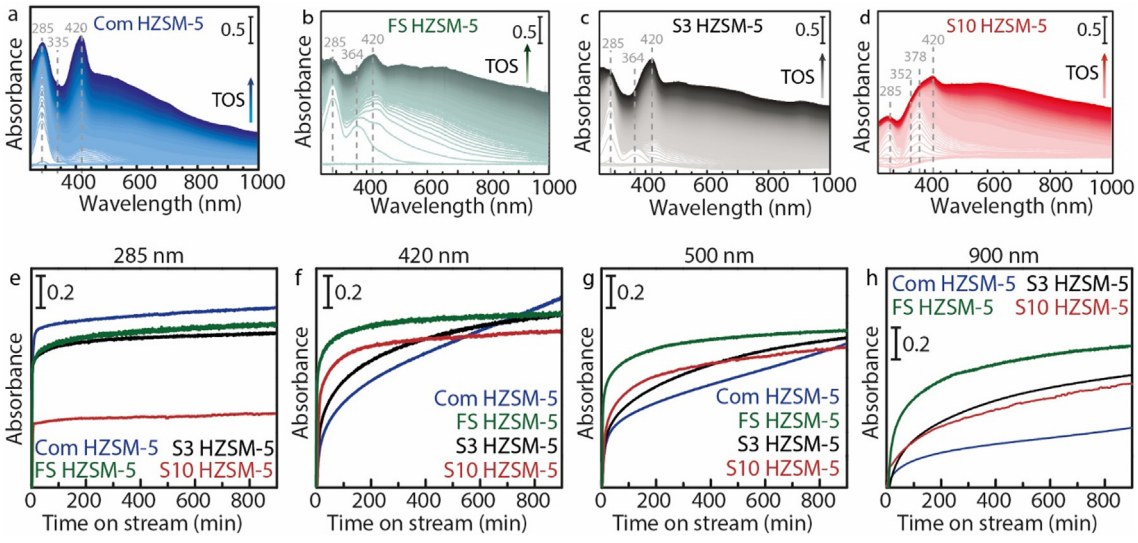

Fig. 7. Coke formation and zeolite deactivation studies using *operando* UV–Vis diffuse reflectance spectroscopy. a-d) *Operando* UV–Vis diffuse reflectance spectroscopy (DRS) data of the Com HZSM-5 (blue), FS HZSM-5 (green), S3 HZSM-5 (black) and S10 HZSM-5 (red). d-g) Absorbance at specific wavelengths (i.e., 285, 420, 500 and 900 nm, respectively) versus time-on-stream (TOS).

waste-derived zeolite ZSM-5 materials, tested in the MTH reaction, revealed a high catalytic performance. However, an increase in the impurities content resulted in a decrease in methanol conversion, while at the same time increasing the propylene and ethylene yield. Hence, altering the amount of impurities has a great impact on the product selectivity of waste-derived zeolite ZSM-5 for the MTH reaction, which was achieved by altering the reaction mechanism, as proven by *operando* UV–Vis DRS.

Declaration of Competing Interest

The authors declare that they have no known competing financial interests or personal relationships that could have appeared to influence the work reported in this paper.

Acknowledgements

This research has received funding from the European Union's EU Framework Program for Research and Innovation Horizon 2020 under Grant Agreement No. 721385 (MSCA-ETN SOCRATES - https://etn-socrates.eu/). The authors would like to thank Donglong Fu and Ioannis Nikolopoulos, both from Utrecht University (UU), for their assistance in the zeolite synthesis and the fruitful scientific discussions. Remco Dalebout, Kristiaan Helfferich, Suzan Schoemaker and Joren Dorresteijn, all from (UU), are acknowledged for performing the Ar physisorption measurements.

References

[1] R. Anuwattana, K.J. Balkus, S. Asavapisit, P. Khummongkol, Conventional and microwave hydrothermal synthesis of zeolite ZSM-5 from the cupola slag, Micropor. Mesopor. Mater. 111 (2008) 260–266.
[2] M.I. Epov, N.V. Yurkevich, S.B. Bortnikova, Y.G. Karin, O.P. Saeva, Analysis of mine waste by geocheimical and geophysical methods (a case study of the mine tailing dump of the Salair ore-processing plant), Russ. Geol. Geophys. 58 (2017) 1543–1552.
[3] P. Altinkaya et al., Leaching of trace amounts of metals from flotation tailings in cupric chloride solutions, Mining, Metall. Explor. 36 (2019) 335–342.
[4] M.M. Ramakokovhu, H. Kasaini, R.K.K. Mbaya, Leaching characteristics of upgraded copper flotation tailings, Int. J. Mater. Metall. Eng. 6 (2012) 1933–1937.
[5] M. Benzaazoua, B. Bussière, M. Kongolo, J. McLaughlin, P. Marion, Environmental desulphurization of four Canadian mine tailings using froth flotation, Int. J. Miner. Process. 60 (2000) 57–74.
[6] J. Cabala, E. Teper, L. Teper, E. Malkowski, A. Rostanski, Mineral composition in rhizosphere of plants grown in the vicinity of a Zn-Pb ore flotation tailings pond. Preliminary study, *Acta Biol. Cracoviensia Ser. Bot.* 46 (2004) 65–74.
[7] Y.R. Lee et al., Synthesis of nanoporous materials via recycling coal fly ash and other solid wastes: A mini review, Chem. Eng. J. 317 (2017) 821–843.
[8] M. Yoldi, E.G. Fuentes-Ordoñez, S.A. Korili, A. Gil, Zeolite synthesis from industrial wastes, Micropor. Mesopor. Mater. 287 (2019) 183–191.
[9] B. Deka, K.G. Bhattacharyya, Using coal fly ash as a support for Mn(II), Co(II) and Ni(II) and utilizing the materials as novel oxidation catalysts for 4-chlorophenol mineralization, J. Environ. Manag. 150 (2015) 479–488.
[10] E. Saputra et al., Red mud and fly ash supported Co catalysts for phenol oxidation, Catal. Today 190 (2012) 68–72.
[11] K. Srivastava, V. Devra, A. Rani, Fly ash supported vanadia catalyst: An efficient catalyst for vapor phase partial oxidation of toluene in a micro-reactor, Fuel Process. Technol. 121 (2014) 1–8.
[12] D. Jain, C. Khatri, A. Rani, Fly ash supported calcium oxide as recyclable solid base catalyst for Knoevenagel condensation reaction, Fuel Process. Technol. 91 (2010) 1015–1021.
[13] J. Park, G.D. Saratale, S.-K. Cho, S. Bae, Synergistic effect of Cu loading on Fe sites of fly ash for enhanced catalytic reduction of nitrophenol, Sci. Total Environm. 705 (2020) 134544.
[14] G. Li et al., Reaction mechanism of low-temperature selective catalytic reduction of NO_x over Fe-Mn oxides supported on fly-ash-derived SBA-15 molecular sieves: Structure-activity relationships and in situ DRIFT analysis, J. Phys. Chem. C 122 (2018) 20210–20231.
[15] G. Li et al., Novel synthesis of fly-ash-derived Cu-loaded SAPO-34 catalysts and their use in selective catalytic reduction of NO with NH_3, Green Energy Environ. 4 (2019) 470–482.
[16] R.N.M. Missengue et al., Transformation of South African coal fly ash into ZSM-5 zeolite and its application as an MTO catalyst, Comptes Rendus Chim. 20 (2017) 78–86.
[17] R.N.M. Missengue et al., Conversion of South African coal fly ash into high-purity ZSM-5 zeolite without additional source of silica or alumina and its application as a methanol-to-olefins catalyst, Catalysts 8 (2018) 124.
[18] M. Chareonpanich, T. Namto, P. Kongkachuichay, J. Limtrakul, Synthesis of ZSM-5 zeolite from lignite fly ash and rice husk ash, Fuel Process. Technol. 85 (2004) 1623–1634.
[19] M. Popova et al., VOC oxidation and CO_2 adsorption on dual adsorption/catalytic system based on fly ash zeolites, Catal. Today 357 (2020) 518–525.
[20] S. Boycheva et al., Studies on non-modified and copper-modified coal ash zeolites as heterogeneous catalysts for VOCs oxidation, J. Hazard. Mater. 361 (2019) 374–382.
[21] E.A. Uslamin et al., Gallium-promoted HZSM-5 zeolites as efficient catalysts for the aromatization of biomass-derived furans, Chem. Eng. Sci. 198 (2019) 305–316.
[22] J. Goetze, B.M. Weckhuysen, Spatiotemporal coke formation over zeolite ZSM-5 during the methanol-to-olefins process as studied with: Operando UV-vis spectroscopy: A comparison between H-ZSM-5 and Mg-ZSM-5, Catal. Sci. Technol. 8 (2018) 1632–1644.
[23] J. Goetze et al., Insights into the activity and deactivation of the methanol-to-olefins process over different small-pore zeolites as studied with operando UV-vis spectroscopy, ACS Catal. 7 (2017) 4033–4046.
[24] M.S. Oncel, A. Muhcu, E. Demirbas, M. Kobya, A comparative study of chemical precipitation and electrocoagulation for treatment of coal acid drainage wastewater, J. Environ. Chem. Eng. 1 (2013) 989–995.
[25] C.A. Cravotta, Dissolved metals and associated constituents in abandoned coal-mine discharges, Pennsylvania, USA. Part 2: Geochemical controls on constituent concentrations, Appl. Geochem. 23 (2008) 203–226.
[26] J. Weitkamp, L. Puppe (Eds.), Catalysis and Zeolites; Fundamentals and Applications, Springer, Berlin, 1999.
[27] E.G. Derouane, G. Zelimir, Role of selected synthesis variables in nucleation and growth of zeolite ZSM-5, J. Solid State Chem. 64 (1986) 296–304.
[28] A. Nastro, Z. Gabelica, P. Bodart, J.B. Nagy, Competitive roles of alkali and TPA cations during nucleation and growth of ZSM-5 zeolite, Stud. Surf. Sci. Catal. 19 (1984) 131–137.
[29] A. Nastro, L.B. Sand, Growth of larger crystals of ZSM-5 in the system 4(TPA) 2O–38(NH2), 2O–x(Li, Na, K)2-O-Al2O3-59SiO2-750H2O, Zeolites 3 (1983) 57–62.
[30] M. Thommes et al., Physisorption of gases, with special reference to the evaluation of surface area and pore size distribution (IUPAC Technical Report), Pure Appl. Chem. 87 (2015) 1051–1069.
[31] Y. Liu et al., Improved para-xylene selectivity in meta-xylene isomerization over ZSM-5 crystals with relatively long b-axis length, ChemCatChem 5 (2013) 1517–1523.
[32] L. Meng et al., A dual-templating synthesis strategy to hierarchical ZSM-5 zeolites as efficient catalysts for the methanol-to-hydrocarbons reaction, J. Catal. 361 (2018) 135–142.
[33] L. Meng, B. Mezari, M.G. Goesten, E.J.M. Hensen, One-step synthesis of hierarchical ZSM-5 using cetyltrimethylammonium as mesoporogen and structure-directing agent, Chem. Mater. 29 (2017) 4091–4096.
[34] T. Weissenberger et al., Hierarchical ZSM-5 catalysts: The effect of different intracrystalline pore dimensions on catalyst deactivation behaviour in the MTO reaction, ChemCatChem 12 (2020) 2461–2468.
[35] R.M. Mohamed, H.M. Aly, M.F. El-Shahat, I.A. Ibrahim, Effect of the silica sources on the crystallinity of nanosized ZSM-5 zeolite, Micropor. Mesopor. Mater. 79 (2005) 7–12.
[36] C. Hammond et al., Aqueous-phase methane oxidation over Fe-MFI zeolites; Promotion through isomorphous framework substitution, ACS Catal. 3 (2013) 1835–1844.
[37] K. Sadowska et al., Desilication of highly siliceous zeolite ZSM-5 with NaOH and NaOH/tetrabutylamine hydroxide, Micropor. Mesopor. Mater. 168 (2013) 195–205.
[38] K. Góra-Marek et al., IR studies of Fe modified ZSM-5 zeolites of diverse mesopore topologies in the terms of their catalytic performance in NH_3-SCR and NH_3-SCO processes, Appl. Catal. B Environ. 179 (2015) 589–598.
[39] J. Li et al., Nanocrystal H[Fe, Al]ZSM-5 zeolites with different silica-alumina composition for conversion of dimethyl ether to gasoline, Fuel Process. Technol. 191 (2019) 104–110.
[40] R.P. Vélez, U. Bentrup, W. Grünert, A. Brückner, The role of NO_2 in the fast NH_3-SCR of NO_x: A combined in situ FTIR and EPR spectroscopic study, Top. Catal. 60 (2017) 1641–1652.
[41] M.S. Kumar, M. Schwidder, W. Grünert, A. Brückner, On the nature of different iron sites and their catalytic role in Fe-ZSM-5 $DeNO_x$ catalysts: New insights by a combined EPR and UV/VIS spectroscopic approach, J. Catal. 227 (2004) 384–397.
[42] K.G. Padmalekha et al., $DeNO_x$ active iron sites in iron loaded ZSM-5 – a multitechnique analysis of a complex heterogeneous catalyst based on Mössbauer spectroscopy, Hyperfine Interact. 238 (2017) 80.
[43] P. Fejes et al., Attempts to produce uniform Fe(III) siting in various Fe-content ZSM-5 zeolites determination of framework/extra-framework ratio of Fe(III) in zeolites by EPR and Mössbauer spectroscopy, Appl. Catal. A Gen. 242 (2003) 247–266.
[44] D.E. De Vos, B.M. Weckhuysen, T. Bein, ESR fine structure of manganese ions in zeolite A detects strong variations of the coordination environment, J. Am. Chem. Soc. 118 (1996) 9615–9622.

[45] S.S. Yakushkin, S.N. Trukhan, V.F. Yudanov, G.A. Bukhtiyarova, O.N. Martyanov, Features of EPR application to systems containing paramagnetic centers and ferromagnetic nanoparticles, Appl. Magn. Reson. 38 (2010) 495–500.
[46] I. Yarulina et al., Structure–performance descriptors and the role of Lewis acidity in the methanol-to-propylene process, Nat. Chem. 10 (2018) 804–812.
[47] X. Jiang et al., Conversion of methanol to light olefins over nanosized [Fe, Al] ZSM-5 zeolites: Influence of Fe incorporated into the framework on the acidity and catalytic performance, Micropor. Mesopor. Mater. 263 (2018) 243–250.
[48] Y. Wang, Y. Chang, M. Liu, A. Zhang, X. Guo, A facile strategy to prepare shaped ZSM-5 catalysts with enhanced para-xylene selectivity and stability for toluene methylation: The effect of in situ modification by attapulgite, Molecules 24 (2019) 3462.
[49] G.T. Whiting, A.D. Chowdhury, R. Oord, P. Paalanen, B.M. Weckhuysen, The curious case of zeolite-clay/binder interactions and their consequences for catalyst preparation, Faraday Discuss. 188 (2016) 369–386.
[50] H.S. Kamaluddin, S.N. Basahel, K. Narasimharao, M. Mokhtar, H-ZSM-5 materials embedded in an amorphous silica matrix: Highly selective catalysts for propylene in methanol-to-olefin process, Catalysts 9 (2019) 364.
[51] L. Lin et al., Acid strength controlled reaction pathways for the catalytic cracking of 1-butene to propene over ZSM-5, J. Catal. 309 (2014) 136–145.
[52] W. Dai, G. Wu, L. Li, N. Guan, M. Hunger, Mechanisms of the deactivation of SAPO-34 materials with different crystal sizes applied as MTO catalysts, ACS Catal. 3 (2013) 588–596.
[53] K. Hemelsoet et al., Identification of intermediates in zeolite-catalyzed reactions by in situ UV/Vis microspectroscopy and a complementary set of molecular simulations, Chem. Eur. J. 19 (2013) 16595–16606.
[54] Y. Jiang, M. Hunger, W. Wang, On the reactivity of surface methoxy species in acidic zeolites, J. Am. Chem. Soc. 128 (2006) 11679–11692.
[55] M.J. Wulfers, F.C. Jentoft, The role of cyclopentadienium ions in methanol-to-hydrocarbons chemistry, ACS Catal. 4 (2014) 3521–3532.
[56] G.T. Whiting, N. Nikolopoulos, I. Nikolopoulos, A.D. Chowdhury, B.M. Weckhuysen, Visualizing pore architecture and molecular transport boundaries in catalyst bodies with fluorescent nanoprobes, Nat. Chem. 11 (2019) 23–31.
[57] J. Goetze, I. Yarulina, J. Gascon, F. Kapteijn, B.M. Weckhuysen, Revealing lattice expansion of small-pore zeolite catalysts during the methanol-to-olefins process using combined operando X-ray diffraction and UV-vis spectroscopy, ACS Catal. 8 (2018) 2060–2070.
[58] D. Fu, O. van der Heijden, K. Stanciakova, J.E. Schmidt, B.M. Weckhuysen, Disentangling reaction processes of zeolites within single-oriented channels, Angew. Chem. Int. Ed. 59 (2020) 15502–15506.
[59] A.A. Rownaghi, F. Rezaei, J. Hedlund, Uniform mesoporous ZSM-5 single crystals catalyst with high resistance to coke formation for methanol deoxygenation, Micropor. Mesopor. Mater. 151 (2012) 26–33.